

Observation of Microlensing towards the Galactic Spiral Arms. EROS II 2 year survey ^{*}

F. Derue¹, C. Afonso², C. Alard³, J-N. Albert¹, A. Amadon², J. Andersen⁴, R. Ansari¹, É. Aubourg², P. Bareyre⁵, F. Bauer², J-P. Beaulieu⁶, A. Bouquet⁵, S. Char^{7**}, X. Charlot², F. Couchot¹, C. Coutures², R. Ferlet⁶, J-F. Glicenstein², B. Goldman², A. Gould^{8***}, D. Graff^{2,9}, M. Gros², J. Haïssinski¹, J-C. Hamilton⁵, D. Hardin², J. de Kat², A. Kim⁵, T. Lasserre², É. Lesquoy², C. Loup⁶, C. Magneville², B. Mansoux¹, J-B. Marquette⁶, É. Maurice¹⁰, A. Milsztajn², M. Moniez¹, N. Palanque-Delabrouille², O. Perdureau¹, L. Prévot¹⁰, N. Regnault¹, J. Rich², M. Spiro², A. Vidal-Madjar⁶, L. Vigroux², S. Zylberajch²

The EROS collaboration

in memory of Sergio Char

- ¹ Laboratoire de l'Accélérateur Linéaire, IN2P3-CNRS, Université de Paris-Sud, B.P. 34, 91898 Orsay Cedex, France
- ² CEA, DSM, DAPNIA, Centre d'Études de Saclay, 91191 Gif-sur-Yvette Cedex, France
- ³ DASGAL, INSU-CNRS, 77 avenue de l'Observatoire, 75014 Paris, France
- ⁴ Astronomical Observatory, Copenhagen University, Juliane Maries Vej 30, 2100 Copenhagen, Denmark
- ⁵ Collège de France, LPCC, IN2P3-CNRS, 11 place Marcellin Berthelot, 75231 Paris Cedex, France
- ⁶ Institut d'Astrophysique de Paris, INSU-CNRS, 98 bis Boulevard Arago, 75014 Paris, France
- ⁷ Universidad de la Serena, Facultad de Ciencias, Departamento de Física, Casilla 554, La Serena, Chile
- ⁸ Department of Astronomy, Ohio State University, Columbus, Ohio 43210, U.S.A.
- ⁹ Department of Physics, Ohio State University, Columbus, Ohio 43210, U.S.A.
- ¹⁰ Observatoire de Marseille, INSU-CNRS, 2 place Le Verrier, 13248 Marseille Cedex 04, France

Received 13/03/1999, accepted

Abstract. We present the analysis of the light curves of 8.5 million stars observed during two seasons by EROS (Expérience de Recherche d'Objets Sombres), in the Galactic plane away from the bulge. Three stars have been found that exhibit luminosity variations compatible with gravitational microlensing effects due to unseen objects. The corresponding optical depth, averaged over four directions, is $\bar{\tau} = 0.38^{+0.53}_{-0.15} \times 10^{-6}$. All three candidates have long Einstein radius crossing times (~ 70 to 100 days). For one of them, the lack of evidence for a parallax or a source size effect enabled us to constrain the lens-source configuration. Another candidate displays a modulation of the magnification, which is compatible with the lensing of a binary source.

The interpretation of the optical depths inferred from these observations is hindered by the imperfect knowledge of the distance to the target stars. Our measurements are compatible with expectations from simple galactic models under reasonable assumptions on the target distances.

Send offprint requests to: M. Moniez: Moniez@lal.in2p3.fr;
see also our WWW server at URL :

<http://www.lal.in2p3.fr/EROS/eros.html>

^{*} This work is based on observations made at the European Southern Observatory, La Silla, Chile.

^{**} deceased

^{***} Alfred P. Sloan Foundation Fellow

Key words: Galaxy: halo – Galaxy: kinematics and dynamics – Galaxy: stellar content – Galaxy: structure – (*Cosmology:*) gravitational lensing

1. Introduction

Since the seminal paper of Bohdan Paczyński 1986, observations have demonstrated that gravitational microlensing is an efficient tool to investigate the Milky Way structure. After the first detections of microlensing effects towards the Large Magellanic Cloud (Alcock et al. 1993; Aubourg et al. 1993) and towards the Galactic bulge (Udalski et al. 1993; Alcock et al. 1995), searches for microlensing have entered an active era. The results of recent campaigns of observations are somewhat difficult to interpret. The negative search for short duration events and the rarity of long duration events found towards the Magellanic Clouds (Ansari et al. 1996; Alcock et al. 1997a; Palanque-Delabrouille et al. 1998 and Alcock et al. 1998) imply that only heavy dark compact objects ($M > 10^{-2}M_{\odot}$) could account for a significant fraction ($\gtrsim 25\%$) of the halo mass required to explain the rotation curve of our galaxy. On the other hand, the optical depth measured in the Galactic bulge direction (Udalski et al. 1994;

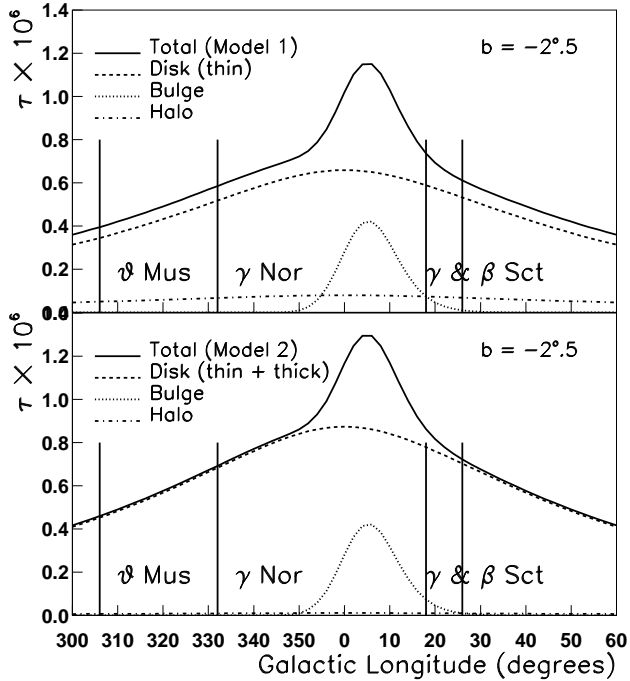


Fig. 1. Expected optical depth ($\times 10^6$) up to 7 kpc for the different components of the Milky Way as a function of the Galactic longitude at $b = -2.5$ for two models of the Galaxy (see Table 4). The 4 directions towards the spiral arms are indicated. Notice that at this Galactic latitude the bulge and disc contributions are already reduced by a factor $\simeq 2$ with respect to zero latitude; moreover, the bulge contribution also changes dramatically with the distance to the target (here assumed to be at 7 kpc, while the Galactic Centre is at 8.5 kpc).

Alcock et al. 1997b) appears to be significantly larger than expected from the contributions of the disc, the bulge and the halo. The latter measurements have led to the hypothesis of an ellipsoidal structure of the Galactic bulge. It is thus important to disentangle the different contributions to this large optical depth. The estimate of the disc contribution can be refined by investigating lines of sight that do not go through the hypothetic ellipsoidal structure (see Fig. 1). Therefore the EROS team has chosen to search for microlensing not only towards the Magellanic Clouds and the Galactic bulge, but also in four regions of the Galactic plane, located at a large angle from the Galactic Centre.

2. The observations

2.1. Data taking

Since July 1996 the EROS team has been using at La Silla observatory the MARLY telescope (1 m, $f/5$) with a dichroic beam-splitter allowing simultaneous imaging of a $0.7(\alpha) \times 1.4(\delta)$ field in EROS-visible and EROS-red wide

passbands. Photons are collected by two cameras, each equipped with a 2×4 mosaic of $2K \times 2K$ LORAL CCDs (Bauer et al. 1997). In this analysis, seven sub-fields are considered per image because one of our 16 CCDs is not operational. The pixel size is 0.6 arcsec, and the median global seeing is 2 arcsec. CCDs are read-out in parallel in approximately 50 s, during which the telescope moves towards the next field to be imaged. After acquisition by the VME system, raw data are reduced by DEC-Alpha workstations using flat-field images taken at the beginning of the night. The DLT tapes produced are shipped to the CCPN (IN2P3 computing centre, CNRS) in Lyons, France, for subsequent processing.

The two EROS passbands are nonstandard. EROS-red passband is centered on $\bar{\lambda} = 762$ nm with a full width half maximum $\Delta\lambda \simeq 200$ nm, and EROS-visible passband is centered on $\bar{\lambda} = 600$ nm with $\Delta\lambda \simeq 200$ nm. Our calibration studies show that the corresponding magnitudes R_{EROS} and V_{EROS} are close to Cousins I and Johnson R to ± 0.3 magnitudes. These R_{EROS} and V_{EROS} magnitudes will be used all along this article.

2.2. The targets

Four different directions are monitored in the Galactic plane, away from the bulge, totalizing 29 fields which have a high stellar density, and cover a wide range of Galactic longitude. We refer to them as β & γ Sct, γ Nor and θ Mus. Table 1 gives the coordinates and available data related to the monitored directions; Fig. 2 displays the positions of the fields in Galactic coordinates and Fig. 3 shows the observation periods and average time sampling. The exposure times of 2 and 3 minutes were chosen to optimize the global sensitivity of the photometric measurements taken during microlensing magnifications (a compromise between the number of measurements and their precision, see Mansoux 1997).

By contrast with the Magellanic Clouds, the distance distribution of the monitored stars is imperfectly known, and should *a priori* vary with the limiting magnitude. In our detection conditions, the populations of stars used to obtain the optical depths given in Sect. 4.1 below are those described by the colour-magnitude diagrams of Fig. 4. An analysis of these diagrams has shown that their content is dominated by a population of source stars located ~ 7 kpc away, undergoing an interstellar extinction of about 3 magnitudes (see Mansoux 1997 for more details). This distance estimate is in rough agreement with the distance to the spiral arms deduced from Georgelin et al. 1994 and Russeil et al. 1998, and will be used in this paper.

3. The search for lensed stars

3.1. Data processing and analysis

Light curves have been produced from the sequences of images using the specific software PEIDA (*Photométrie*

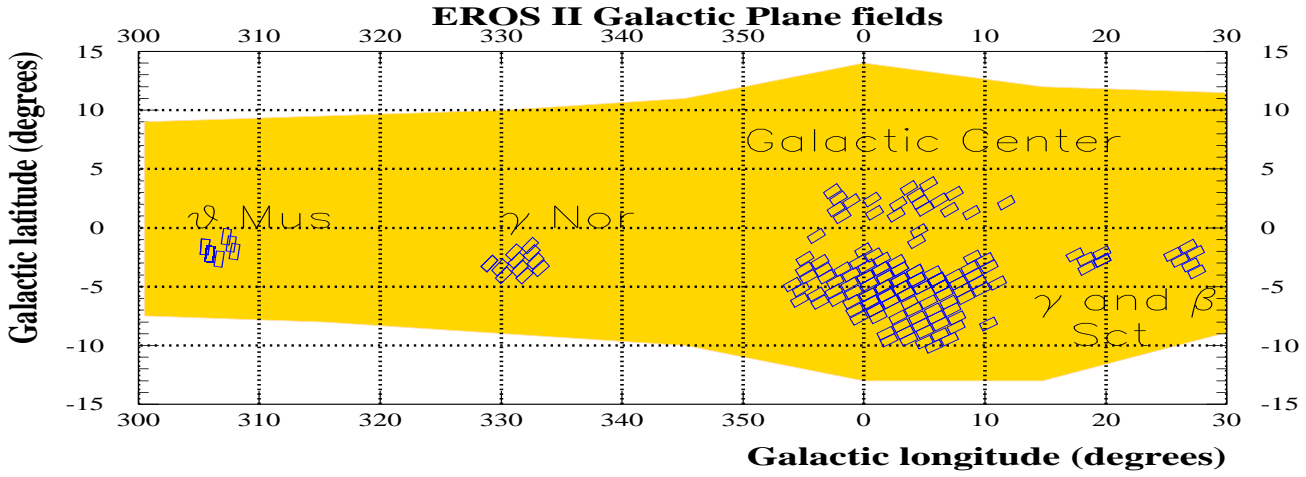


Fig. 2. Map of the Galactic plane fields (Galactic coordinates) monitored by EROS for the microlensing search. The shaded area represents the shape of the Galaxy. We have indicated our Galactic Centre fields and the 4 directions towards the arms.

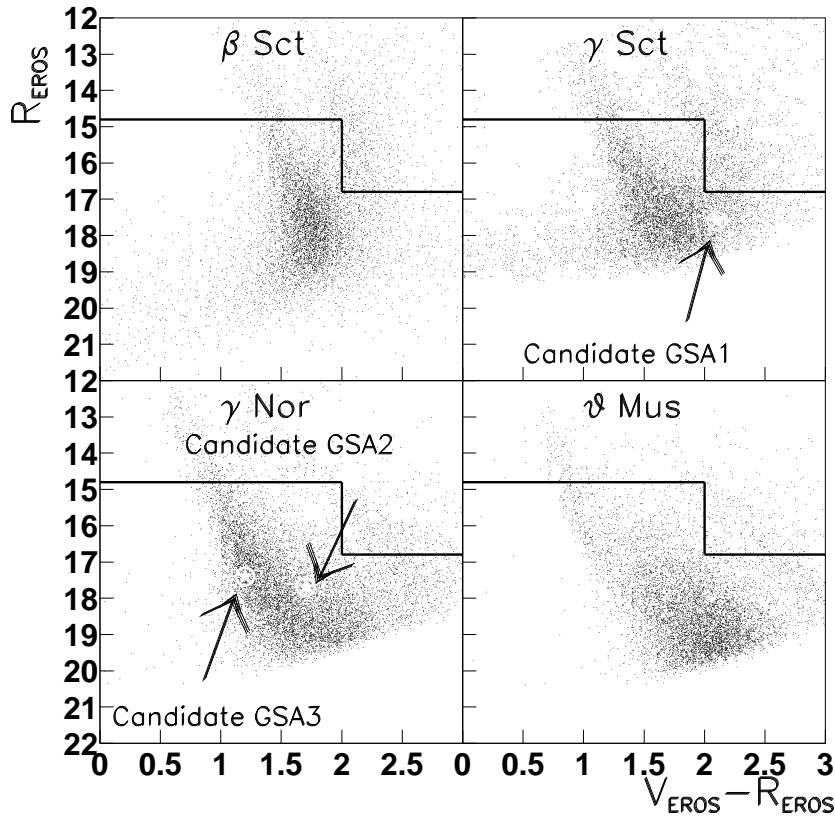


Fig. 4. Colour-magnitude diagrams (R_{EROS} vs $V_{EROS} - R_{EROS}$) for the stars monitored by EROS in the directions of β & γ Sct, γ Nor and θ Mus. The boxes drawn in the upper corners correspond to the zones excluded from the search. The positions of the 3 candidates are indicated.

Table 1. Description of the 29 fields monitored in the spiral arms program. This table gives the fields centres, the averaged number of measurements and the number of light curves analysed in this article. Field gn401 has not been studied yet.

Field number	α (h:m:s) J2000	δ (d:m:s) J2000	# of meas.	stars (million)
Scutum (β Sct)			53	1.96
bs300	18:43:22.0	-07:40:53	55	0.33
bs301	18:43:27.0	-06:13:42	52	0.23
bs302	18:46:16.0	-07:22:45	50	0.32
bs303	18:46:20.0	-05:55:35	50	0.28
bs304	18:49:21.0	-06:45:51	54	0.43
bs305	18:52:26.0	-06:35:44	53	0.37
Scutum (γ Sct)			51	1.70
gs200	18:28:03.0	-14:51:06	55	0.32
gs201	18:31:15.0	-14:14:38	52	0.30
gs202	18:31:33.0	-12:48:53	49	0.29
gs203	18:34:22.0	-14:31:39	50	0.34
gs204	18:34:28.0	-13:04:31	50	0.45
Norma (γ Nor)			100	3.01
gn400	16:09:45.0	-53:07:03	100	0.37
gn401	16:18:22.0	-51:44:43	-	-
gn402	16:14:57.0	-53:04:35	101	0.25
gn403	16:22:28.0	-52:06:20	108	0.30
gn404	16:19:09.0	-53:26:38	106	0.29
gn405	16:26:52.0	-52:21:02	111	0.22
gn406	16:23:54.0	-53:43:53	106	0.33
gn407	16:31:31.0	-52:28:44	107	0.22
gn408	16:28:42.0	-53:51:58	92	0.22
gn409	16:15:51.0	-54:48:45	90	0.26
gn410	16:20:30.0	-55:04:18	82	0.23
gn411	16:09:37.0	-55:10:07	90	0.32
Musca (θ Mus)			66	1.77
tm500	13:27:04.0	-63:02:18	65	0.31
tm501	13:31:18.0	-63:34:41	64	0.33
tm502	13:34:52.0	-64:10:30	68	0.33
tm503	13:23:58.0	-64:59:52	64	0.29
tm504	13:12:12.0	-64:06:49	70	0.23
tm505	13:16:15.0	-64:40:50	65	0.28
Total				8.44

et *Étude d'Images Destinées à l'Astrophysique*), designed to extract photometric information in crowded fields (Ansari 1996). Figure 5 shows the mean point-to-point relative dispersion of the measured fluxes along those light curves as a function of R_{EROS} and V_{EROS} . A systematic search for microlensing events has been performed on a set of about 300,000 stars per field (8.5×10^6 light curves in total), with an average of 70 measurements in the V_{EROS} and R_{EROS} colours (between July 1996 and November 1997).

This search is based on procedures and criteria similar to the ones developed for the EROS microlensing search in the SMC data (Palanque-Delabrouille et al. 1998). These criteria are designed to select microlensing events using

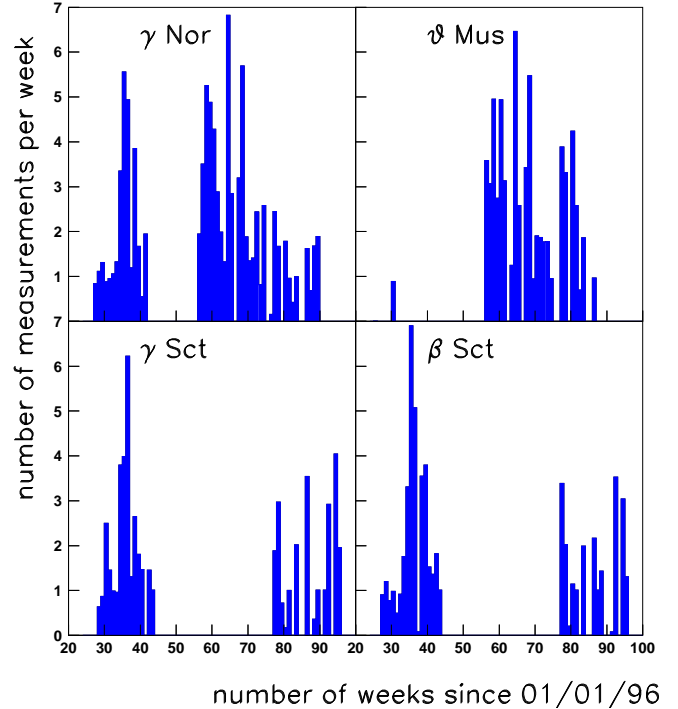


Fig. 3. Time sampling for each direction monitored towards the spiral arms, in number of measurements per week. γ Nor is monitored between January and October, θ Mus is observed between January and August. β & γ Sct are monitored between May and November.

the expected characteristics of their light curves (one single peak, simultaneous in the visible and red bands, with a known shape), and to reject variable stars (rejection of stars lying in regions of the colour-magnitude diagrams mostly populated by variable stars, and requirement for the stability of the curve outside the peak). They are also tuned to be loose enough to avoid rejection of non-standard microlensing events, which have a different peak shape.

The main difference from the SMC analysis is the rejection against variable stars from the instability strip and against red giant variables. Unlike the Magellanic Clouds case where the positions of these populations in the colour-magnitude diagram are known *a priori*, the scatter and imperfect knowledge of the distances and reddenings of our target stars make our colour-magnitude cut somewhat empirical. In particular, its acceptance is different from one field to another (see the excluded regions in Fig. 4).

3.2. The efficiency of the analysis

To determine the efficiency of each selection criterion, we have applied them to Monte-Carlo generated light curves, obtained from a representative sample of the observed light curves, on which we superimpose randomly generated

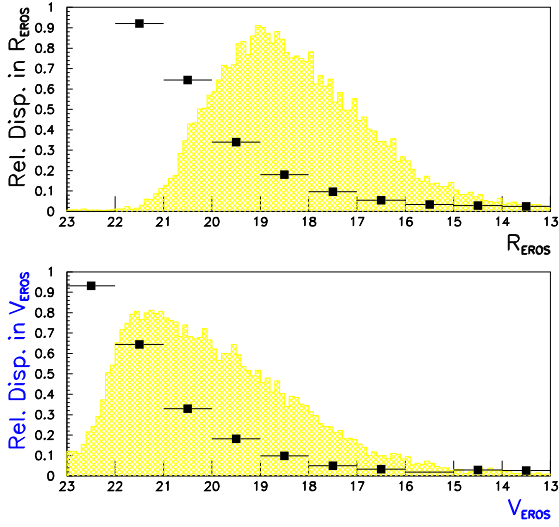


Fig. 5. Relative frame to frame average dispersion of the luminosity measurements versus R_{EROS} (upper panel) and V_{EROS} (lower panel), for stars with at least 50 reliable measurements for each colour. This dispersion is taken as an estimator of the mean photometric precision. The superimposed hatched histograms show the magnitude distribution of the stars in EROS bands.

microlensing effects. The microlensing parameters are uniformly drawn in the following intervals: impact parameter expressed in Einstein radius unit $u_0 \in [0, 2]$, maximum magnification time in a research period T_{obs} starting 50 days before the first observations and ending 50 days after the last observations¹, and Einstein radius crossing time $\Delta t \in [1, 150]$ days. The analysis efficiency (or sampling efficiency) shown in Fig. 6 is relative to a set of unblended stars. Blending of a lensed star results in the mixing of unmagnified light with the expected light curve. The efficiency of the search and the reconstruction of the lensing parameters are hence affected by this distortion. On the other hand, the set of stars that could undergo a detectable lensing effect is larger than the sample of the monitored stars, and the expected number of events is also affected. These effects, which are usually included as corrections to the sampling efficiency, are not taken into account in the present article and will require a specific study. For other targets (SMC, LMC), we have determined the correction of the detection rate due to blending to be less than 10-20% (Renault 1996; Palanque-Delabrouille 1997).

¹ Outside this domain of parameters, the detection efficiency is negligible.

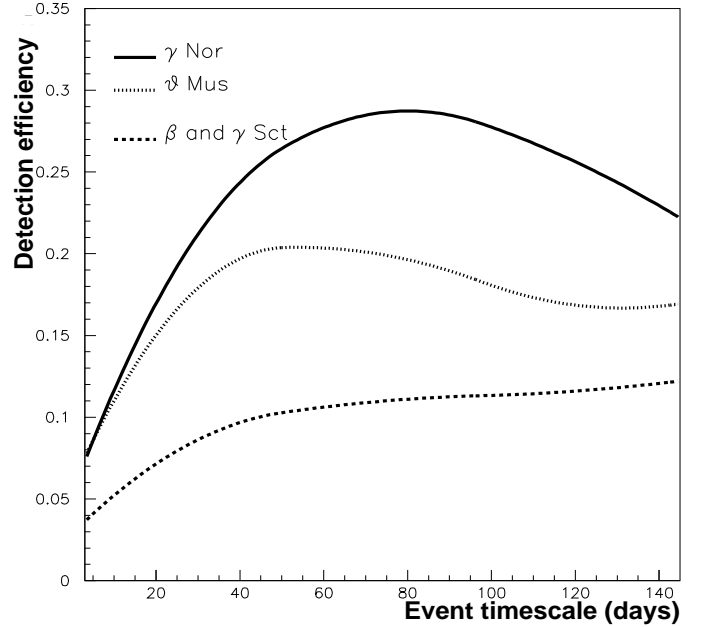


Fig. 6. EROS microlensing detection efficiency $\epsilon(\Delta t)$ as a function of Δt , the Einstein radius crossing time. $\epsilon(\Delta t)$ is the ratio of the number of simulated events, satisfying the selection criteria with duration Δt , with any u_0 and any date of peak magnification within the research period (650 days), to the number of events generated with $u_0 \leq 1$.

3.3. Results of the selection

Three light curves satisfy all the requirements and are hereafter named candidates and labelled GSA1 to 3. Figures 7, 8 and 9 show the light curves of each candidate and Table 2 contains their characteristics. Measurements taken after Jan 1st, 1998 (date 2922) are shown, although they were not used in the selection.

4. Optical depth and event timescales

4.1. Optical depth

The optical depth towards a pointlike source is defined as the fraction of time during which it undergoes a lensing magnification larger than 1.34. For a given target the measured optical depth τ is computed from:

$$\tau = \frac{1}{N_{obs} T_{obs}} \frac{\pi}{2} \sum_{events} \frac{\Delta t}{\epsilon(\Delta t)},$$

where N_{obs} is the number of monitored stars in the target, T_{obs} is the duration of the search period (650 days for this 2 year analysis) and $\epsilon(\Delta t)$ is the average detection efficiency normalized to the microlensing events with impact

Table 2. Characteristics of the 3 microlensing candidates

Candidate	EROS2-GSA1	EROS2-GSA2	EROS2-GSA3
field	γ <i>Sct</i>	γ <i>Nor</i>	γ <i>Nor</i>
Coordinates of star (J2000)	$\alpha = 18\text{h}29\text{m}09.0\text{s}$ $\delta = -14^\circ 15' 09''$	$\alpha = 16\text{h}11\text{m}50.2\text{s}$ $\delta = -52^\circ 56' 49''$	$\alpha = 16\text{h}16\text{m}26.7\text{s}$ $\delta = -54^\circ 37' 49''$
Galactic coordinates	$b = -1.^\circ 67$ $l = 17.^\circ 75$	$b = -1.^\circ 17$ $l = 330.^\circ 49$	$b = -2.^\circ 86$ $l = 329.^\circ 82$
R_{EROS}	17.6	17.7	17.4
V_{EROS}	19.7	19.4	18.6
Date of maximum magnification	Aug. 3 rd , 1996	Mar. 26 th , 1997	Oct. 7 th , 1997
Julian Day -21,447,891.5	2408.6 ± 0.1	2642.9 ± 0.2	2806.2 ± 1.1
Einstein radius crossing time $\Delta t = R_E/V_T$ (days)	73.5 ± 1.4	98.3 ± 0.9	70.0 ± 2.0
Max. magnification	26.5 ± 0.6	3.05 ± 0.02	1.89 ± 0.01
Impact parameter (in R_E)	0.0378 ± 0.001	0.342 ± 0.002	0.593 ± 0.007
χ^2 of best fit	185.7/163 d.o.f.	551/425 d.o.f.	445/427 d.o.f.
Remarks	$M_{lens} > 4.6 \times 10^{-3} M_\odot$ at 95% C.L. (see text)	binary source fit period 98 days (see text)	

Table 3. Contribution of the candidates to the optical depth τ assuming the sources to be 7 kpc away. In the case of θ Mus we give a 95% C.L. upper limit on the optical depth contribution from events with $\Delta t = 80$ days ($\epsilon(80 \text{ days}) = 18\%$).

Target Direction	Scutum		Norma	Musca
	β <i>Sct</i>	γ <i>Sct</i>	γ <i>Nor</i>	θ <i>Mus</i>
$\langle b \rangle$	$-2.^\circ 5$	$-2.^\circ 6$	$-2.^\circ 7$	$-1.^\circ 8$
$\langle l \rangle$	$27.^\circ 0$	$18.^\circ 6$	$331.^\circ 2$	$306.^\circ 4$
Events detected	none	GSA1	GSA2 & 3	none
Δt (days)	-	73	98 & 70	(80)
$\epsilon(\Delta t)(\%)$	-	10	27	(18)
$\tau(\text{event})(\times 10^6)$	-	1.02	0.29 & 0.21	-
$\bar{\tau}(\text{target})(\times 10^6)$	-	0.47	0.5	< 1.82 at 95% CL
$\bar{\tau}$ averaged over the 4 directions ($\times 10^6$)				$0.38^{+0.53}_{-0.15}$

parameter $u_0 < 1$, whose maximum magnification takes place within the research period. The contribution of the candidates to the optical depth is given in Table 3.

We have modeled the Galaxy in two different ways using three components: a central bulge, a disc and a dark halo. The density distribution for the bulge - a barlike triaxial model - is taken from Dwek et al. 1995 model G2 (in cartesian coordinates):

$$\rho_{Bulge} = \frac{M_{Bulge}}{8\pi abc} e^{-r^2/2}, \quad r^4 = \left[\left(\frac{x}{a} \right)^2 + \left(\frac{y}{b} \right)^2 \right]^2 + \frac{z^4}{c^4},$$

where M_{Bulge} is the bulge mass, and a, b, c are the length scale factors. The bar major axis is inclined at an angle of 15° with respect to the Sun-Galactic Centre line.

We compare our measurements with the predictions of two models with extreme disk contributions (here the main structure involved in microlensing). The first one has a “thin” disc and a standard isotropic and isothermal halo (Model 1) with a density distribution given in spherical coordinates by:

$$\rho(r) = \rho_{h\odot} \frac{R_\odot^2 + R_c^2}{r^2 + R_c^2},$$

where $\rho_{h\odot}$ is the local halo density, $R_\odot = 8.5$ kpc is the distance between the Sun and the Galactic Centre, and $R_c = 5$ kpc is the Halo “core radius”. The matter distribution in the disc is modeled in cylindrical coordinates by a double exponential (see e.g Bienaymé et al. 1987 and Schaeffer et al. 1998):

$$\rho_{thin}(R, z) = \frac{\Sigma_{thin}}{2H_{thin}} \exp\left(\frac{-(R - R_\odot)}{R_{thin}}\right) \exp\left(\frac{-|z|}{H_{thin}}\right),$$

Σ_{thin} is the column density of the disc at the Sun position, H_{thin} is the height scale and R_{thin} is the length scale of the disc.

The second model (Model 2) has a “thin” and a “thick” disc, and a very light halo. Both models share the same bulge contribution. The model parameters are summarized in Table 4. Fig. 1 shows the expected optical depth up to 7 kpc as a function of longitude for both models, at the average latitude of our fields $b = -2.5^\circ$. As the main contribution comes from the thin disc (about 90%), variations of the optical depth from field to field due to the range of 2 to 3° in latitude can reach $\simeq 30\%$ in the case of γ Nor, and $\simeq 20\%$ for the other targets.

The expected optical depth, averaged over the four directions, is 0.60×10^{-6} for model 1, and 0.70×10^{-6} for

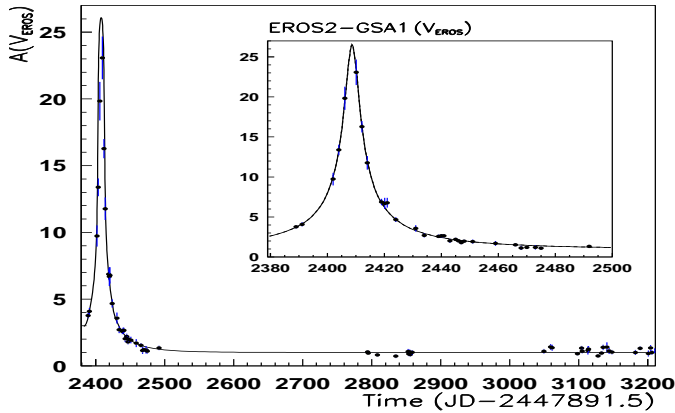
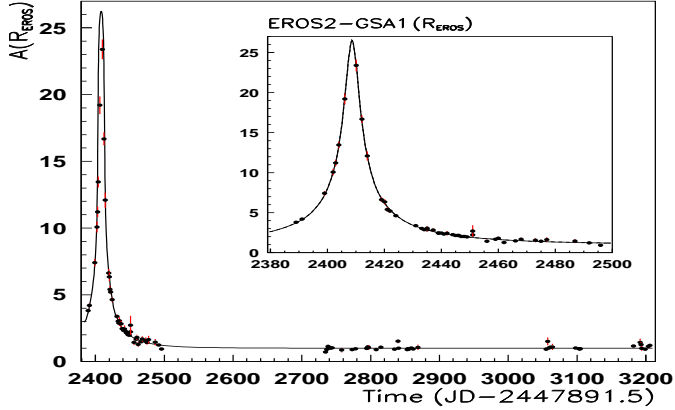


Fig. 7. Magnification curves of the microlensing candidate GSA1 in the direction of γSct . The fitted standard microlensing curve is superimposed (solid line).

model 2. These estimates vary by 50% if the average distance of the sources is changed by 2kpc, or if the parameter Σ_{thin} is changed by $25M_{\odot}/\text{pc}^2$. The measured optical depth, averaged over the four directions is:

$$\bar{\tau} = 0.38_{-0.15}^{+0.53} \times 10^{-6}.$$

The confidence interval reported here takes into account Poisson fluctuations and the possible event timescale variations inside the range [71, 98] days. The comparison of Fig. 1 with Table 3 also shows that the measured optical depths in the four directions are compatible with the predictions of both models.

4.2. Microlensing event timescales

The duration of the three events is long (~ 80 days in average). Fig. 10 shows the expected event duration distribution towards γNor within the framework of model 1. This distribution is obtained assuming the following mass functions and kinematical characteristics:

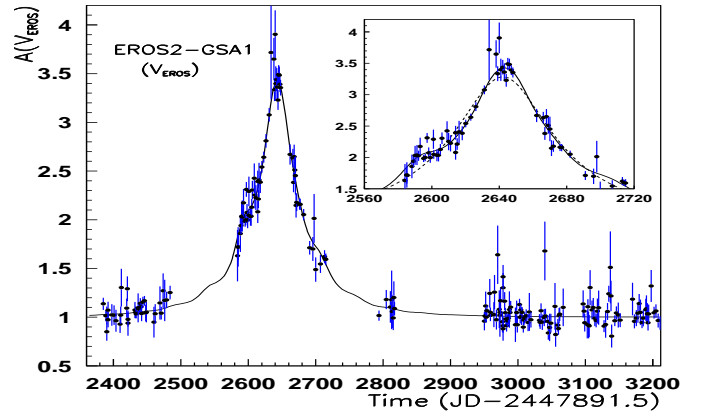
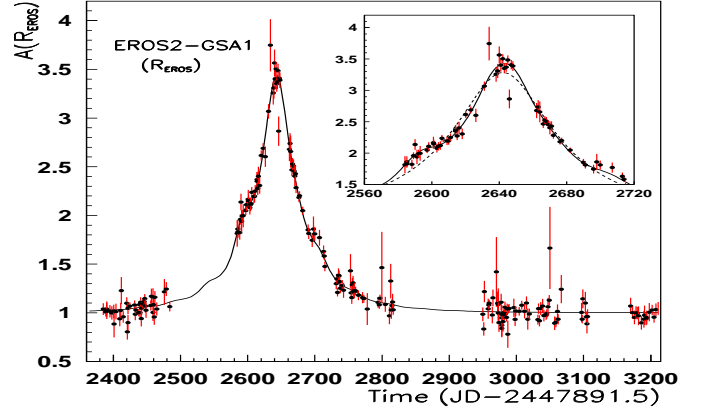


Fig. 8. Magnification curves of the microlensing candidate GSA2 in the direction of γNor . The solid line shows the fitted microlensing curve taking into account the modulation due to a dominant source orbiting in a binary system with period $P_0 = 98$ days. The dashed line corresponds to the best standard microlensing fit.

- We assume that lenses belonging to the (non-rotating) halo have the same mass ($0.5M_{\odot}$); their velocities transverse to the line of sight of disc stars follow a Boltzmann distribution with a dispersion of $\sim 150\text{km/s}$. Thus the expected duration of microlensing events is small (see Fig. 10).
- For lenses belonging to the bulge, the mass function is taken from Richer et al. 1992 and the velocities transverse to the line of sight of disc stars also follow a Boltzmann distribution with a dispersion of $\sim 110\text{km/s}$. The expected rate of microlensing events due to this structure towards the direction considered in Fig. 10 (γNor) is found to be negligible.
- The disc lenses mass function is taken from Gould 1997, which is derived from HST observations. Disc lenses are subject to a similar global rotation as the observer and the sources (Brand & Blitz 1993). We assume a negligible particular motion of the monitored

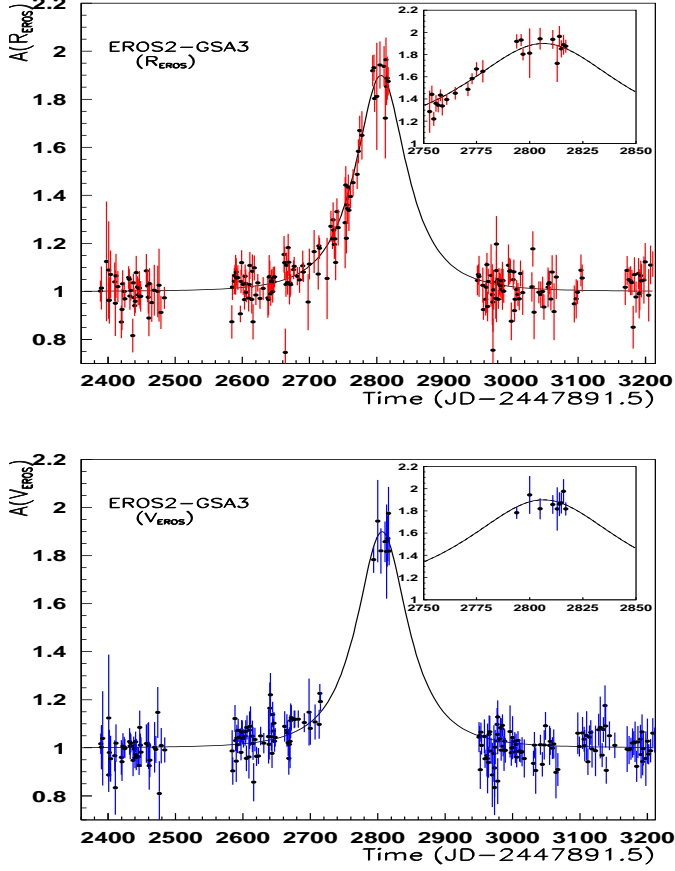


Fig. 9. Magnification curves of the microlensing candidate GSA3, in the direction of γ Nor.

sources with respect to the spiral arms, because they are probably young stars. Following Griest 1991, the motion of the Sun relative to the Local Standard of Rest is taken as ($v_{\odot R} = 9$, $v_{\odot \theta} = 11$, $v_{\odot z} = 16$) (in km/s); the velocity dispersions of the lens population are expected to be ($\sigma(V_R) = 40$, $\sigma(V_\theta) = 30$, $\sigma(V_z) = 20$) (in km/s). As the disc lenses have a low velocity relative to the line of sight, disc-disc events have longer timescales, as can be seen on Fig. 10.

Assuming that all three lenses belong to the halo leads to large probable masses ($> 2M_\odot$). As such high mass lenses would be visible stars that we do not observe (dismissing the unlikely possibility that the three could be neutron stars), the disc-disc lensing hypothesis is more probable. This hypothesis could also explain the fact that 4 events over the 45 found by the MACHO Collaboration towards the Galactic Centre (see Alcock et al. 1997b) have a timescale > 50 days, significantly larger than the mean for the whole sample (21 days). Indeed, the contribution of these 4 events to the total optical depth is about 0.6×10^{-6} , which is compatible with the expectation of the disc lensing contribution ($\sim 0.7 \times 10^{-6}$ for Model 1).

Table 4. Parameters of the galactic models used in this article.

	Parameter	Model 1	Model 2
Bulge	a (kpc)	1.49	
	b (kpc)	0.58	
	c (kpc)	0.40	
	$M_{bulge} (\times 10^{10} M_\odot)$	2.1	
Thin disc	$\Sigma (M_\odot \text{pc}^{-2})$	50	
	H (kpc)	0.325	
	R (kpc)	3.5	
	$M_{thin} (\times 10^{10} M_\odot)$	4.3	
Thick disc	$\Sigma (M_\odot \text{pc}^{-2})$	-	35
	H (kpc)	-	1.0
	R (kpc)	-	3.5
	$M_{thick} (\times 10^{10} M_\odot)$	-	3.1
Halo	$\rho_{h\odot} (M_\odot \text{pc}^{-3})$	0.008	0.003
	R_c (kpc)	5.0	5.0
	M in 60 kpc ($10^{10} M_\odot$)	51	7
Predictions	$\rho_\odot (M_\odot \text{pc}^{-3})$	0.085	0.098
	V_{rot} at sun (km s $^{-1}$)	211	222
	V_{rot} at 20 kpc	203	180
	V_{rot} at 60 kpc	200	140

5. Detailed analyses of the candidates

Detailed analyses have been performed on GSA1 and GSA2 candidates, whose light curves are sufficiently sampled. For this purpose, we have used all available data on the candidates (i.e. three years of observations).

5.1. Candidate EROS2-GSA1

Candidate GSA1 exhibits a large magnification ($A_{peak} > 25$ at 95% C.L.) with no detectable blending² and no detectable parallax effect (Gould 1992). Despite the small impact parameter, no evidence for a distortion of the curve due to the non-zero size of the lensed source is found. A fitting procedure allows one to put an upper limit to the ratio of the angular stellar radius θ_* to the angular Einstein radius θ_E of the lens:

$$\frac{\theta_*}{\theta_E} = \frac{\theta_*}{\sqrt{\frac{4GM}{c^2} \frac{1-x}{xD}}} < 0.066 \text{ at } 95\% \text{ C.L.},$$

where M is the lens mass, D the distance of the observer to the source and xD its distance to the lens. From the position of the source in the colour-magnitude diagram we can assume that its temperature is comparable to or lower than that of the Sun. We then obtain:

$$\frac{\theta_*}{\theta_\odot \text{ at } 10 \text{ pc}} > 10^{(V_{EROS\odot}^{abs} - V_{EROS*}^{app})/5},$$

² Fits including more than 10% blending are excluded at 95% C.L. Moreover, since the magnification curves are the same in both colours, the amplified star and an hypothetical blending star would have to have -by chance- the same colour.

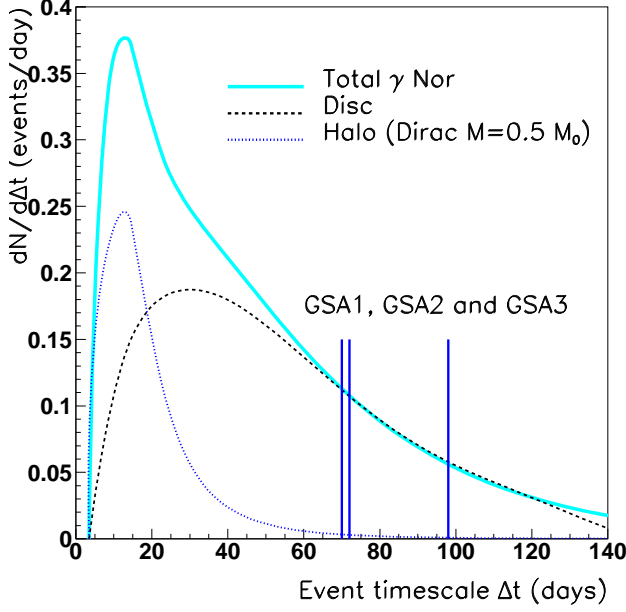


Fig. 10. Δt distribution of the events expected during the search period T_{obs} per 10^7 monitored stars towards γNor , within model 1. This distribution takes into account the detection efficiency $\epsilon(\Delta t)$. The durations of the three candidates are marked. Notice that the bulge contribution is negligible.

where the apparent magnitude $V_{EROS\star}^{app}$ should be corrected for the interstellar extinction. Ignoring this correction leads to the conservative limit $\theta_\star > 2.37 \times 10^{-12}$ rad, implying that $\theta_E > 3.6 \times 10^{-11}$ rad and that the angular proper motion of the deflector:

$$\mu \text{ (km/s/kpc)} = 3.57 \times 10^{11} \frac{\theta_E \text{ (rad)}}{\Delta t \text{ (days)}} > 0.17 \text{ at } 95\% \text{ C.L.}$$

Assuming the interstellar extinction to be 3 magnitudes (see Sect. 2.2) leads to $\theta_\star > 9.42 \times 10^{-12}$ rad, implying that $\theta_E > 1.43 \times 10^{-10}$ rad and:

$$\mu > 0.69 \text{ km/s/kpc at } 95\% \text{ C.L.}$$

Since the typical expected value (based on Galactic kinematics) is $\mu \simeq 4$ km/s/kpc, this limit does not probe the expected range of parameter space.

On the other hand, the standard microlensing fit is satisfactory, and taking into account the possibility of a parallax effect does not result in a significantly better fit. We can then infer a lower limit on \tilde{r}_E , the size of the Einstein ring projected from the source onto the observer's plane:

$$\tilde{r}_E = \frac{\theta_E x D}{(1-x)} > 1.33 \text{ AU at } 95\% \text{ C.L.}$$

This implies a lower limit on the projected speed of the lens onto the local transverse plane:

$$\tilde{v} = \tilde{r}_E / \Delta t > 31.6 \text{ km/s at } 95\% \text{ C.L.}$$

Since typical values expected for this quantity are of the order of $\tilde{v} \simeq 100$ km/s, it is clear that this is not a very constraining limit either. Fig. 11 shows the excluded area for the tip of the 2-dim. vector \vec{v} in the local transverse plane. The lower limit we find for the modulus \tilde{v} (and \tilde{r}_E) is relatively small, because the best parallax fit, which is not significantly better than a standard fit (183.7/161 d.o.f. compared with 185.7/163 d.o.f.), is obtained for $\vec{v} = (-17.1, -31.1)$ km/s in the frame of Fig. 11. This special configuration produces a distorted light curve which diverges only marginally from the standard fitted curve, and only during periods where the measurements are not very precise.

From the definitions of θ_E and \tilde{r}_E one gets the relation:

$$M = \frac{c^2}{4G} \tilde{r}_E \theta_E = \frac{c^2}{4G} \tilde{v} \mu \Delta t^2,$$

from which we derive a lower limit on the lens mass by combining the two constraints from finite size and parallax analysis, i.e. at 95% C.L.:

$$\begin{aligned} M &> 1.2 \times 10^{-3} M_\odot \text{ ignoring interstellar extinction,} \\ M &> 4.6 \times 10^{-3} M_\odot \text{ with 3 magnitudes of extinction.} \end{aligned}$$

Note that this limit is independent of the lens and source distances to the observer. The fact that this lower limit is so much smaller than the expected mass for such lenses follows immediately from the fact that each limit from which it is derived is not probing the expected range of kinematic parameters. Fig. 12 shows the excluded areas in the M versus x plane, from the finite size study and the parallax analysis, assuming the source to be located 7 kpc away. Exclusion curves for the two hypotheses on the interstellar absorption are shown. A better characterization of the lensed source should allow one to refine these preliminary studies.

Finally, a limit on the lens luminosity can be derived from the maximum blending limit allowed by the fit. At 95% C.L., the apparent magnitude of the lens is at least 2.5 magnitudes above the measured baseline magnitude, i.e. $R_{EROS} > 20.1$ and $V_{EROS} > 22.2$.

5.2. Candidate EROS2-GSA2

GSA2 has residuals to a standard microlensing fit which clearly exhibit a modulation; a period of ~ 54 days is found in the residuals of the standard fit during the magnification. On the other hand, taking into account a possible parallax effect does not significantly improve this fit. Furthermore, we know that the lensing of a periodic variable star would produce a modulation of the light curve whose amplitude should follow the magnification. As we do not

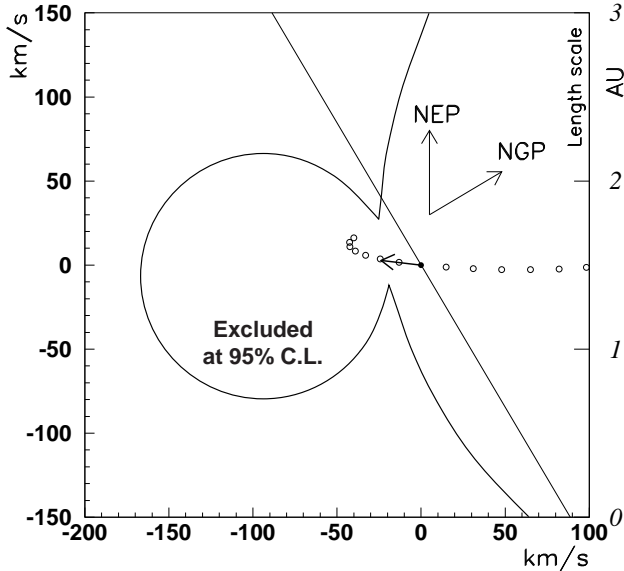


Fig. 11. Excluded area for the tip of the 2-dim. vector \vec{v} in the local transverse plane. The smallest speed compatible with the observations corresponds to a deflector with a velocity oriented towards the lower spike. The arrow shows the earth projected velocity at the maximum magnification time. The straight line is the intersection of the Galactic plane. The projection of the earth trajectory is indicated by the open circles, starting 60 days before maximum, ending 70 days after maximum, with 10 days spacing (right scale in AU). NEP is the North Ecliptic Pole direction, NGP is the North Galactic Pole direction.

detect a significant modulation in the non-magnified part of the light curve, the most probable origin of this modulation is that one dominant luminous source or two sources orbit around the centre of gravity of a binary system, inducing a wobbling of the line of sight with respect to the trajectory of the lens³. In this configuration, a modulation of the light curve is expected to occur only during the

³ This type of configuration has been studied by Griest & Hu 1992, Sazhin & Cherepashchuk 1994 and Han & Gould 1997, and was already mentioned in our earlier article (Ansari et al. 1995).

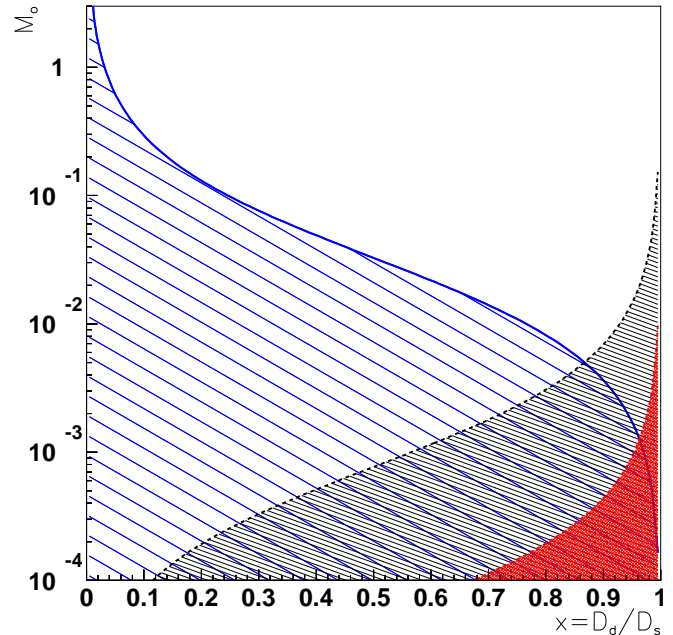


Fig. 12. 95% C.L. exclusion diagram from the parallax analysis and from the finite source size study for the candidate EROS2-GSA1. The lower curve in the right part is the conservative limit ignoring interstellar absorption, the higher curve corresponds to a 3 magnitude absorption. These curves assume the source to be located 7 kpc away. If the source is assumed to be at some other distance D , one has to scale the increasing functions by the factor $D/(7 \text{ kpc})$, and the decreasing function by $(7 \text{ kpc})/D$.

lensing peak. We obtain equally satisfactory fits for two classes of circular binary systems (with at best $\chi^2 = 551$ for 425 d.o.f., to be compared with 876 for 439 d.o.f. for a standard microlensing fit).

The first class includes systems with a dominant source orbiting with a period $P_o \sim 51$ days, and with the projected semi-axis $\rho = ax/R_E \sim 0.04$ ⁴. The second class corresponds to systems with two luminous stars orbiting with a period $P_o \sim 98$ days, with luminosity and mass ratios around 1/3-1/2, and a projected distance between the two components of about $\rho = ax/R_E \simeq 0.4$. Given the domain of values for x and R_E , these parameters are compatible with physically acceptable masses of the binary satisfying Kepler's third law. Many more configurations can fit the observations if we consider systems with elliptic orbits. A spectroscopic study of the source is under way in order to test its binarity. If the source proves to be

⁴ Fits which are slightly less good can be obtained with larger periods, but in this case only the first shoulder (around date=2600) is correctly matched.

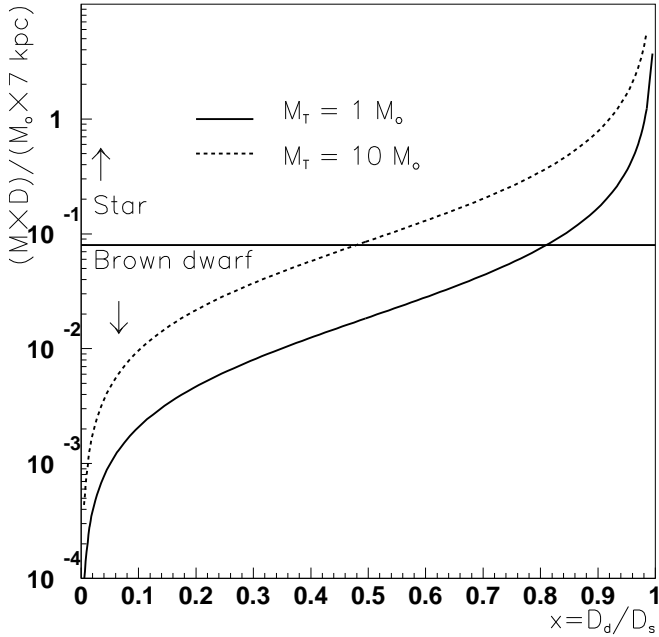


Fig. 13. Relation between $M_{lens} \times D$ and x assuming a binary system with $P_o = 100$ days, $\rho = 0.4$ and a total mass M_T of $1M_\odot$ or $10M_\odot$.

a spectroscopic binary, then one can get a good estimate or constraint on the angular Einstein radius θ_E (and then on the angular proper motion of the lens μ).

Expressing the Einstein radius and Kepler's third law in the relation $\rho = ax/R_E$ leads to:

$$\frac{M_{lens}}{M_\odot} \frac{D}{7 \text{ kpc}} \sim 6.7 \cdot 10^{-6} \left[\frac{P_o}{1 \text{ day}} \right]^{\frac{4}{3}} \left[\frac{M_T}{M_\odot} \right]^{\frac{2}{3}} \rho^{-2} \frac{x}{1-x}.$$

Fig. 13 illustrates this relation between $M_{lens} \times D$ and x assuming the source to be a binary system with $P_o = 100$ days, with $\rho = 0.4$ and with two different hypotheses for the mass M_T of the system.

6. Conclusion

We have searched for microlensing events with durations ranging from a few days to a few months in four Galactic disc fields lying 18° to 55° from the Galactic Centre. We find three events that can be interpreted as microlensing effects due to massive compact objects. Their long duration favours the interpretation of lensing by objects belonging to the disc instead of the halo. The average optical depth measured towards the four directions is $\bar{\tau} = 0.38_{-0.15}^{+0.53} \times 10^{-6}$. Assuming the sources to be 7 kpc away, the expected optical depths from two different galactic models vary from 0.60 to 0.70×10^{-6} , in agreement with our measurement.

One event displays a modulation of the magnification which is compatible with the lensing of a binary source. More information about the configuration of this possible binary source, and about the lens mass acting on the strongly amplified source, are expected from complementary observations. No evidence for parallax and blending effects has been found.

The observations continues towards the spiral arms. More accurate measurements should be obtained with the increase of statistics (Derue 1999), allowing one to estimate the disc contribution to the optical depth towards the bulge and the Magellanic Clouds.

Acknowledgements. We are grateful to D. Lacroix and the technical staff at the Observatoire de Haute Provence and to A. Baranne for their help in refurbishing the MARLY telescope and remounting it in La Silla. We are also grateful for the support given to our project by the technical staff at ESO, La Silla. We thank J.F. Lecoite for assistance with the on-line computing. We wish to thank also C. Nitschelm for his contribution to the data taking.

References

- Alcock C., Akerlof C.W., Allsman R.A. et al. (MACHO Coll., 1993, Nat 365, 621.
- Alcock C., Allsman R.A., Axelrod T.S. et al. (MACHO Coll.), 1995, ApJ 445, 133.
- Alcock C., Allsman R.A., Alves D. et al. (MACHO Coll.), 1997a, ApJ 486, 697.
- Alcock C., Allsman R.A., Alves D. et al. (MACHO Coll.), 1997b, ApJ 479, 119.
- Alcock C., Allsman R.A., Alves D. et al. (EROS Coll., MACHO Coll.), 1998, ApJ 499, L9.
- Ansari R., 1996, Vistas in Astronomy 40, 519
- Ansari R., Cavalier F., Couchot F. et al. (EROS Coll.), 1995, A&A 299, L21.
- Ansari R., Cavalier F., Moniez M. et al. (EROS Coll.), 1996, A&A 314, 94.
- Aubourg É., Bareyre P., Bréhin S. et al. (EROS Coll.), 1993, Nat 365, 623.
- Bauer F., Afonso C., Albert J-N et al. (EROS Coll.), 1997, Proceedings of the "Optical Detectors for Astronomy" workshop, ESO.
- Bienaymé O., Robin A., Crézé M., 1987, A&A 180, 94.
- Brand J., Blitz L., 1993, A&A 275, 67.
- Derue F., 1999, Ph.D. thesis, CNRS/IN2P3, LAL report 99-14, Université Paris XI Orsay.
- Dwek E., Arendt R.G., Hauser M.G. et al., 1995, ApJ 445, 716.
- Georgelin Y.M, Amram P., Georgelin Y.P. et al., 1994, A&AS 108, 513.
- Gould A., 1992, ApJ 392, 442.
- Gould A., Bahcall J.N., Flynn C., 1997, ApJ 482, 913.
- Griest K., 1991, ApJ 366, 412.
- Griest K., Hu W., 1992, ApJ 397, 362.
- Han C., Gould A., 1997, ApJ 480, 196.
- Mansoux B., 1997, Ph.D. thesis, CNRS/IN2P3, LAL report 97-19, Université Paris 7.
- Paczynski B., 1986, ApJ 304, 1.
- Palanque-Delabrouille N., 1997, Ph.D. thesis, CEA DAP-NIA/SPP report 97-1007, Université Paris 7.

- Palanque-Delabrouille N., Afonso C., Albert J-N. et al. (EROS Coll.), 1998, A&A 332, 1.
- Renault C., 1996, Ph.D. thesis, CEA DAPNIA/SPP report 96-1003, Université Paris 7.
- Richer H.B., Fahlman G.G., 1992, Nature 358, 383.
- Russeil D., Amram P., Georgelin Y.P. et al., 1998, A&AS 130, 119.
- Sazhin M. V., Cherepashchuk A. M., 1994, Astron. Lett., Vol. 20, No. 5, 523.
- Schaeffer R., Méra D. and Chabrier G., 1998, Acta. Phys. Polonica B., Vol. 29, 1905.
- Udalski A., Szymański M., Kaluzny J. et al. (OGLE Coll.), 1993, Act. Astr. 43, 289.
- Udalski A., Szymański M., Stanek K.Z. et al. (OGLE Coll.), 1994, Act. Astr. 44, 165.